Article:

Liu, Q orcid.org/0000-0002-1132-9392, Yang, S, Shen, L et al. (5 more authors) (2020) The effect of hydrogen concentration on the fracture surface of medium Mn steels. Engineering Failure Analysis, 108. 104263. ISSN 1350-6307

https://doi.org/10.1016/j.engfailanal.2019.104263

The effect of hydrogen concentration on the fracture surface of medium Mn steels

Qingyang Liu[a], Shuquan Yang[a], Liancheng Shen[b], Qingjun Zhou[c], Jinxu Li[a],
Yanjing Su[a] , Lijie Qiao[a] , Yu Yan[a,*]

[a] Beijing Advanced Innovation Center for Materials Genome Engineering, Corrosion and Protection Center, Institute for Advanced Materials and Technology, University of Science and Technology Beijing, 100083, China
[b] Division of Technological Sciences, Bureau of Frontier Sciences and Education, Chinese Academy of Sciences (CAS), 100864, China
[c] Baoshan Iron & Steel Co., Ltd, Research Institute, Shanghai 201900, China

*corresponding author.
E-mail address: yanyu@ustb.edu.cn (Y. Yan).
Postal Address: Room 413, Corrosion Building, University of Science and Technology Beijing, No. 30 Xueyuan Road, Beijing 100083, China.

Abstract

To balance good strength and ductility, Medium Mn steels have been considered as the new generation materials used in automotives. However, they show delayed fracture, which is thought to relate to hydrogen. Therefore, in order to understand their mechanical properties with various hydrogen contents, it is very important to assess their safety. In this study, the effect of hydrogen on the mechanical properties of several medium Mn steels (MMSs) with different Mn content and treatments were investigated. For medium Mn steels, the stability of the retained austenite (RA) was examined and the hydrogen permeation test was performed. Austenite, as a barrier to hydrogen diffusion, leads to a tortuous diffusion path, which reduces the diffusion rate of hydrogen in MMSs. Increasing the Mn content increases the volume fraction of RA in the specimen. The stress-strain curves of MMSs were divided into three parts, determined by the stability and content of RA. Slow strain rate tensile tests with hydrogen charging were performed to investigate the behaviour of hydrogen diffusion and the mechanism of hydrogen embrittlement (HE). After the tests, the hydrogen content was measured and the fracture surface was observed and analysed. The phenomenon of HE in steels has been mainly explained based on the mechanisms of hydrogen-enhanced localised plasticity (HELP), hydrogen-enhanced decohesion (HEDE), and hydrogen assisted micro ovoid coalescence (HDMC). Due to the existence of hydrogen, fracture morphology changes from ductile mode to brittle mode. It was also found that under the same strain rate, tensile strength and elongation decrease gradually as hydrogen concentration increases, resulting in final failure.

Key words:

Medium Mn steel; Hydrogen embrittlement; Fracture morphology

1. Introduction

Nowadays, in the automobile industry, weight reduction, energy saving and safety improvement are urgently required. Over the past decades, automobile manufacturers have mainly considered the cost, formability and corrosion resistance of advanced high strength steels (AHSSs) with typically multiphase microstructures. Tensile strength and total elongation (PSE) were called in to value the mechanical properties of AHSSs. Generally, dual phase (DP), martensitic (MART) and transformation-induced plasticity (TRIP) steels are referred to as the first generation AHSSs with a PSE of 10~20GPa•%, while twinning-induced plasticity (TWIP) steels, austenitic steels and lightweight steels with induced plasticity (L–IP) are referred to as the second generation AHSSs with a PSE of 50~70GPa•%. Compared with the first generation AHSSs, higher manufacturing costs and alloying levels severely limited the use of second generation AHSSs. Thus, a third generation AHSSs, with a better strength–ductility combination and lower cost, are urgently needed.

Miller developed the medium Mn steel with 4~10wt% Mn [1]. Mn [1, 2] promotes austenite formation and increases the volume fraction of retained austenite in medium Mn steel at room temperature. Thus, the microstructure of medium Mn steel has a dual phase of ferrite and austenite (typically 20~40 vol%). Due to its good combination of strength and elongation, many scientists have investigated the deformation mechanism and mechanical properties of medium Mn steel [3]. The areas of focus were the tensile behaviours and deformation [3], intercritical annealing conditions [4, 5], fracture characterisation [6], alloying elements [7, 8], the influence of the initial microstructure of α' martensite before intercritical annealing [9-11] and the warm ductility [4] of medium Mn steel.

Hydrogen in high strength steels and alloys has a most common effect, hydrogen embrittlement (HE) [12-14]. Generally, the higher strength materials are more susceptible to HE [15, 16]. It is defined as the process by which strength and ductility of a material can reduced significantly by introduction of hydrogen atom when working on hydrogen environment [16]. Factors which are responsible for susceptibility of materials for HE can be concluded as the synergistic action of materials (nature and surface condition), stress (residual stress and applied strain rate) and environment (concentration of hydrogen, temperature, pressure and solution react with metals) [15, 17, 18]. Liu [19] has explained hydrogen influence on DP, QP and TWIP steels. Depover [20] has investigated the effect of hydrogen charging on the mechanical properties of TRIP, Ferrite Bainitic (FB), DP and High Strength Low Alloy (HSLA) steels, and Han [21] has examined hydrogen embrittlement under intercritically annealed conditions, while hydrogen redistribution under stress-induced diffusion was investigated in structural steel [22].

Medium Mn steel, with various advantages such as excellent strength and ductility, is easily vulnerable to hydrogen embrittlement (HE) [23]. Koyama[24] has reported that the HE susceptibility of medium Mn steels is particularly sensitive to their chemical composition and alloying elements, which affect the stacking fault energy (SFE), austenite phase stability and associated hydrogen segregation on the phase, grain, and twin boundaries. These factors affect micro-stress concentrations and the local diffusible hydrogen content, which acts on the hydrogen-enhanced localised plasticity (HELP) effect [25], on hydrogen-enhanced decohesion (HEDE) [26], on adsorption-induced dislocation emission (AIDE) [27], on hydrogen assisted micro void coalescence (HDMC) [16], as well as on hydrogen-enhanced and strain-induced vacancies (HESIV) formation[28, 29]. Sometime combination of these mechanisms is responsible for degradation and embrittlement of material.

Some researchers studied that the influence of hydrogen content on the tensile properties and fracture modes could be classified into two cases in the high Mn steel [30]. The samples with low diffusible hydrogen content (e.g. 0.33 wt.ppm) showed a ductile fracture while the samples with relatively high diffusible hydrogen content (e.g.1.24 wt.ppm) showed an intergranular fracture. Due to the effect of hydrogen, material became brittle and crack growth happened due to dislocation emission or microvoid coalescence (MVC) [16]. From this view, combination of both dislocation emission and MVC may be responsible for crack growth and ultimately fracture happened in material.

The interaction of hydrogen content, applied stress and fracture morphology for medium Mn steels, however, are rarely reported in the literatures. The study of fracture mode is required for knowledge of how the crack can grow in the material and how the fracture can be influenced due to the effect of hydrogen. Therefore, in this paper, we investigated systematically the role of hydrogen in influencing the fracture surface and mechanical properties of medium Mn steels.

2. Experiment Materials and Methods

2.1 Materials

The medium Mn steels (MMSs) thin plates were supplied by Baoshan Iron & Steel Co., Ltd. In this study, the mechanical properties and hydrogen-induced cracking of medium Mn steels were investigated. The main differences between the three kinds of manganese steel are the Mn content and heat treatment process [31].

The heat treatment detail involved hot-rolled, intercritically batch-annealed and cold-rolled treatment. After steelmaking, the slabs were heated to 1473 K for two hours and hot-rolled in a temperature of 1153 K. Intercritical batch annealing was conducted at 893 K for 12 hours. The thickness for hot-rolled sheets was 2.8mm, consisting of austenite and ferrite. Then, the sheets were pickled and cold-rolled to a thickness of 1.4mm and the thickness conduction was 50pct. The cold-rolled medium Mn steel sheets were heated to 893 K and held for three minutes and 12 hours. The annealing time is relevant to the continuous annealing and batch-annealing processes respectively.

Table **1** lists the chemical composition of the material. The samples prepared in these two annealing conditions are designated as “M7B”, “M7C” and “M10B” respectively, ‘M’ referring to Mn, ‘7’ or ‘10’ meaning the content of Mn, ‘B’ denoting batch annealing and ‘C’ continuous annealing. Transmission electron microscope (TEM) and scanning electron microscopy (SEM) were used to observe the microstructure and fracture morphology.

Table 1 Chemical composition in wt. % of MMSs

Material/element	**C**	**Si**	**Mn**	**Cr**	**Al**	**Fe**
M7B	**0.14**	**0.23**	**7.16**	**0.077**	**0.055**	**balance**
M7C	**0.14**	**0.23**	**7.14**	**0.082**	**0.056**	**balance**
M10B	**0.15**	**0.17**	**10.40**	**0.073**	**1.49**	**balance**

2.2 Hydrogen permeation tests

A double electrolytic cell for hydrogen permeation test was used in this study to investigate the diffusion behaviour of hydrogen in MMSs. In this work, the sample shape was designed like a coin with a diameter of 20mm. Prior to the permeation test, the specimen was ground with SiC paper up to 5,000 grits and, then, ultrasonically cleansed in acetone. In order to avoid the corrosion or passivation of the sample in the solution, nickel coating is usually required on the surface of the sample. The Ni electroplating solution is $250gNiSO_4$-$7H_2O$+$45gNiCl_2$-$6H_2O$+$40gH_3BO_4/L$ with a current density of $10mA/cm^2$ for 60s. The hydrogen-charging solution in the charging side was $0.2molL^{-1}$ NaOH + 0.22 gL^{-1} thiourea (H_2NCSNH_2) with $5mAcm^{-2}$ charging current density at room temperature, approximately 25°C, while the solution in the escaping side was 0.2mol L^{-1} NaOH [22].

2.3 Slow strain rate tensile tests

Slow strain rate tensile tests (SSRT) have gradually become a classical method for studying susceptibility to hydrogen embrittlement (HE), which can be determined by measuring the fracture stress drop, the reduction of the area and the elongation of the material before and after hydrogen charging [22]. The specimen of MMSs used in this study was designed according to ASTM E8, shown in Figure 1. The tensile specimens were 1.5mm thick, and their surfaces were wet-ground with SiC paper up to 2,000 grit, and then ultrasonically cleansed in acetone and ethanol. The strain was recorded from the cross-head displacement. The test strain rate was 1×10^{-6} s^{-1}.

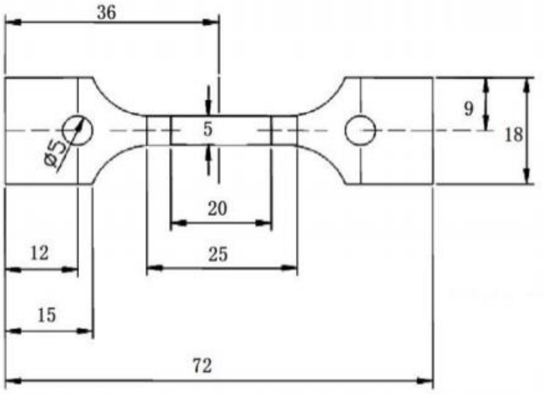

Fig. 1 Schematic diagram of MMSs tensile specimen (dimensions in mm) [32]

For three kinds of MMSs, electrochemical hydrogen charging was implemented in 0.2mol•L^{-1} sulphuric acid (H_2SO_4) and 0.22 g•L^{-1} thiourea solution with a current density of 1mA•cm^{-2}. The specimen was the cathode and the Pt wire was the anode. According to the coefficient of hydrogen diffusion, hydrogen charging time is three hours, eight hours and 24 hours respectively, and hydrogen charging current density is 1mA/cm^2. Only the gauge part of the sample was charged, because other parts were sealed by silica gel. Fracture morphology was observed by a Qyanta FEG 450 scanning electron microscope (SEM), and hydrogen concentration was measured by G4 Phoenix DH at 800 Celsius for 20 min.

Diffusible Hydrogen Analyser G4 PHOENIX, utilising the carrier gas hot extraction method, enables the rapid and automatic determination of diffusible hydrogen in a wide variety of matrices. The analyser is equipped with a rapid heating (and cooling) infrared-heated clamshell furnace (up to 900 Celsius). The quartz tube diameter of 30 mm enables the analysis of large samples like steel sheet strips, as well as weld coupons according to ISO 3690 and AWS A4.3. 800 Celsius was set as the analysis temperature because it can make all hydrogen in the sample escape. Analysis time depended on sample material, weight and analysis temperature, typically 15–20 min.

3. Results and discussion

3.1 Microstructure and tensile behaviour

Fig. 2 presents TEM images of test steels. Due to the ultrafine grained size of test steel, we use the TEM to observe the grain and phase structure more clearly. As is known, MMSs have a dual phase of ferrite and retained austenite. The convex and concave parts of MMSs represent ferrite and retained austenite respectively. M7B is uniformly distributed with globular-shaped ferrite and retained austenite, with a grain size of about 1–3 μm. The microstructure of M7C is mainly distributed with lath-shaped austenite and ferrite, which is mainly due to incomplete annealing. Lengthy batch annealing leads to the recrystallisation of martensite. When it reverts to austenite, long-strip austenite can be combined into block austenite. Continuous annealing for 1–3 minutes can promote the transformation of martensite to austenite, but its microstructure still retains the characteristics of lath martensite.

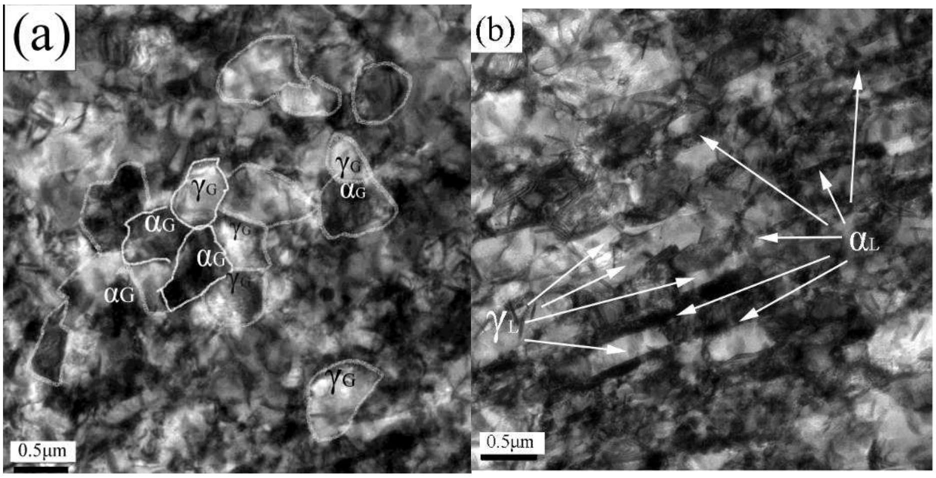

Fig. 2 TEM micrographs of (a)M7B and(b) M7C
α_L and γ_L are lath-shaped ferrite and retained austenite, α_G and γ_L are globular-shaped ferrite and retained austenite.

The engineering stress-strain curve of the MMSs after different annealing processes was shown in Fig. 3. The strain rate in air is $1\times10^{-4}s^{-1}$. The steels exhibit an excellent combination of high strength and ductility; M7B for example measures 745MPa for yield stress, 1133MPa for tensile strength and about 31.3% of total elongation. The product of tensile strength to ductility for M7B is about 35.5 GPa%, for M7C 34.3 GPa% and for M10B 56.1GPa%, listed in Table 2.

Table 2 Mechanical properties of three kinds of MMSs

Steel	Yield stress/MPa	Tensile strength/MPa	Ductility /%	The product of TS and ductility/GPa•%
M7B	745	1133	31.3%	35.5
M7C	1113	1130	30.4%	34.3
M10B	794	1403	40.0%	56.1

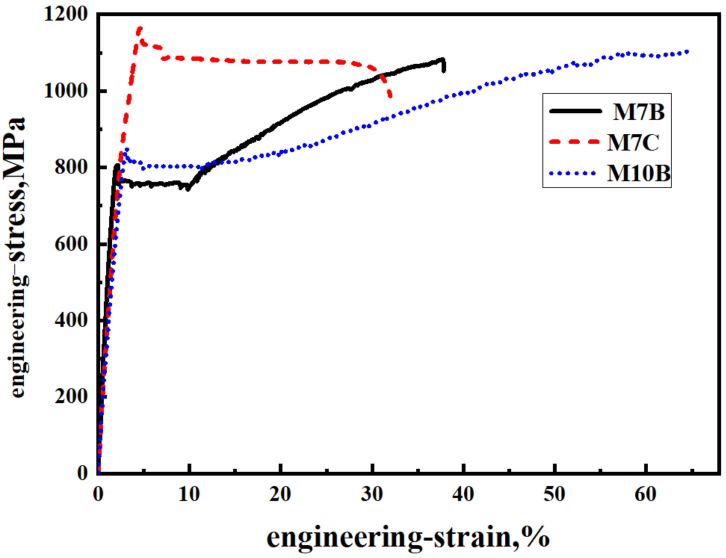

Fig. 3 Engineering stress-strain curves of MMSs

For M7B and M10B, the tensile curve consists of three parts: (1) the elastic strain stage; (2) the stress dropping and yield stage, showing plastic instability; (3) the work hardening stage, whereby stress increases alongside strain. The reasons are as follows: the Cottrell atmosphere leads to stress concentration in the stretching process, and the deformation is not uniform in order to form the yield platform. The stress relaxation mechanism of austenite leads to martensite transformation and produces stress relaxation during the strain process. The stress of M7C reaches a higher level at lower strain, its yield strength is much higher than M7B and M10B, and then the stress is reduced, showing no obvious hardening. This is due to the poor stability of austenite in M7C, which has been transformed into martensite at lower strain conditions in M7C.

Fig. 4 shows the fracture surface of the specimen after SSRT in air. Without necking in the fracture, it shows that uniform deformation mainly occurs within the gauge part. In the MMSs fracture, there are many parallel tear edges, delamination and the distribution of some holes[33]. Some researchers reckoned that during the tensile process delamination was caused by the initiation of micro-cracks at non-metallic inclusions in the ferrite belt, where the micro-cracks combined together and finally forming delamination at the fracture [34]. Others believed that the delamination fracture appeared at half thickness of the cross section, where stress exceeded yield strength to accelerate the occurrence of the crack source in the half thickness of the cross section of the specimen during tension test [35]. It is shown that metastable austenite reduces stress concentration of the interface by the phase transformation during the tensile test [36]. The ferrite alleviates stress concentration at the crack tip to delay crack propagation by deformation.

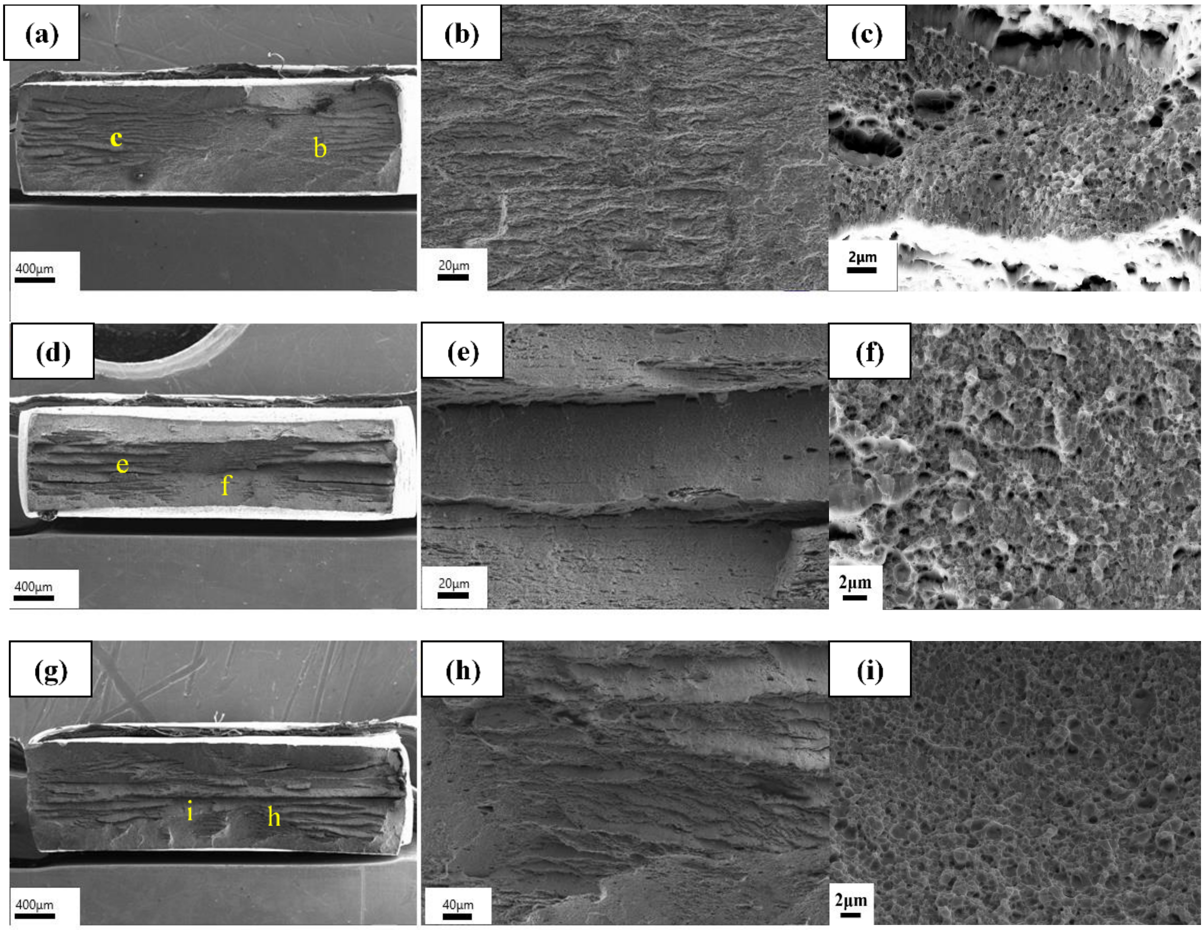

Fig. 4 SEM observation of fracture surfaces (a) (b) (c) for M7B; (d) (e) (f) for M7C; (g) (h) (i) for M10B

3.2 Stability of retained austenite

It has been mentioned that work hardening behaviour is closely related to the martensitic transformation of retained austenite during the tensile process in MMSs. Thus, it is necessary to study the mechanism of phase transformation and the stability of retained austenite during uniaxial tension. The volume fraction of retained austenite (RA) under different plastic strain was measured. Austenite was characterised by an FCC structure and ferrite by a BCC structure [21]. X-ray diffraction can be used to determine the volume fraction of RA in

MMSs. Fig. 5 shows the XRD spectra of MMSs specimens before the tensile test. Based on the integrated intensities of $(200)_\gamma$, $(220)_\gamma$, $(331)_\gamma$, $(211)_\alpha$ and $(200)_\alpha$ diffraction peaks, the calculation of the volume fraction of retained austenite (RA) was performed using the following Eq. (1):

$$V_\gamma = 1.4 I_\gamma / (I_\alpha + 1.4 I_\gamma) \qquad (1)$$

where I_α is the mean integrated intensity of two ferrite diffraction peaks, $(211)_\alpha$ and $(200)_\alpha$; $I\gamma$ is the mean integrated intensity of the three austenite diffraction peaks, $(200)_\gamma$, $(220)_\gamma$ and $(331)_\gamma$. Fig. 6 shows the volume fraction of RA for those samples with different pre-strain of 0 (as received), 5, 10 and 15%.

The stability of RA is expressed in terms of the law of martensitic transformation based on the OC model [37], shown as Eq.(2):

$$K = -\frac{\ln(f_r / f_{r0})}{\varepsilon} \qquad (2)$$

where f_{r0} is the volume fraction of RA before strain and f_r is the volume fraction of RA after strain of ε. K is the stability coefficient of RA. The smaller the K value is, the more stable the RA.

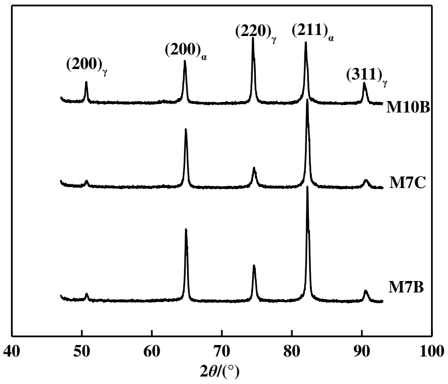

Fig. 5 X-Ray diffraction profiles of MMSs

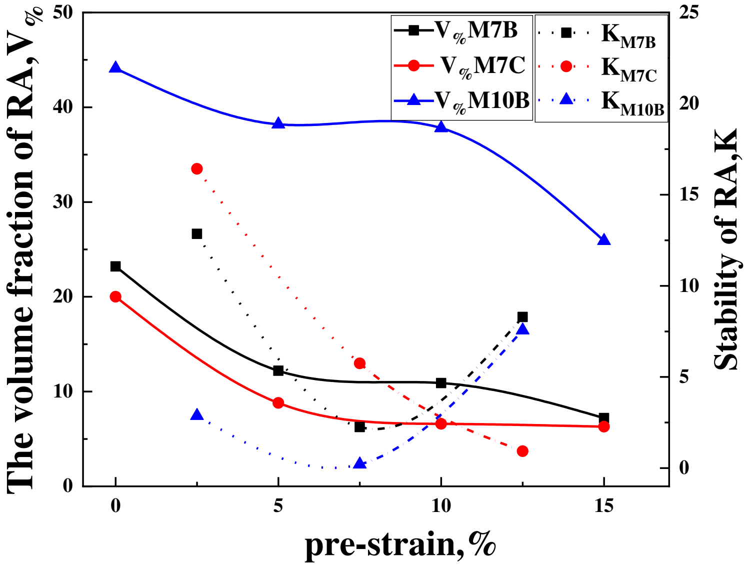

Fig. 6 The volume fraction and stability of RA in MMSs

The solid line and dotted line refer to the volume fraction and stability of RA, respectively.

According to the analysis of the stress strain curve in Fig. 3, pre-strain of 0-0.05 corresponds to the elastic stage and the initial yielding stage, when a large number of RA with poor stability induces martensitic transformation in M7B and M7C. Pre-strain of 0.05–0.10 corresponds to the yielding platform, when the deformation mainly depends on the Lüders strain in the ferrite matrix. M7B and M10B induce obvious work hardening, and martensitic transformation occurs to reduce local stress concentration as pre-strain continues to increase, with the stability coefficient of RA increasing synchronously. Due to the poor stability of austenite for M7C, no obvious work hardening was observed.

The volume fraction and stability of RA under different strain conditions was analysed and calculated by XRD. The stress-strain curve of MMSs can be divided into three stages, which depends on the content and stability of RA. After a short period of continuous annealing treatment, the stability of austenite in M7C is poor, while it has obviously transformed at the beginning of strain. Therefore, no obvious work hardening was observed on the nominal stress – nominal strain curves. The stability of RA in M7B and M10B is relatively high.

3.3 Hydrogen permeation

Fig. 7 is the hydrogen permeation curve of MMSs at room temperature. As can be seen from the curve, the anode current will rise with the hydrogen charging process until a steady state is reached. $t_{0.63}$ was the corresponding time of I_a/I_∞=0.63 to calculate the diffusion coefficient using the following formula:

$$D = \frac{L^2}{6t_{0.63}} \tag{3}$$

The hydrogen diffusion coefficient of MMSs was shown in Table 3. It can be seen that the apparent hydrogen diffusion coefficient of M7B and M7C is similar, but M10B is lower than M7B and M7C by one order of magnitude.

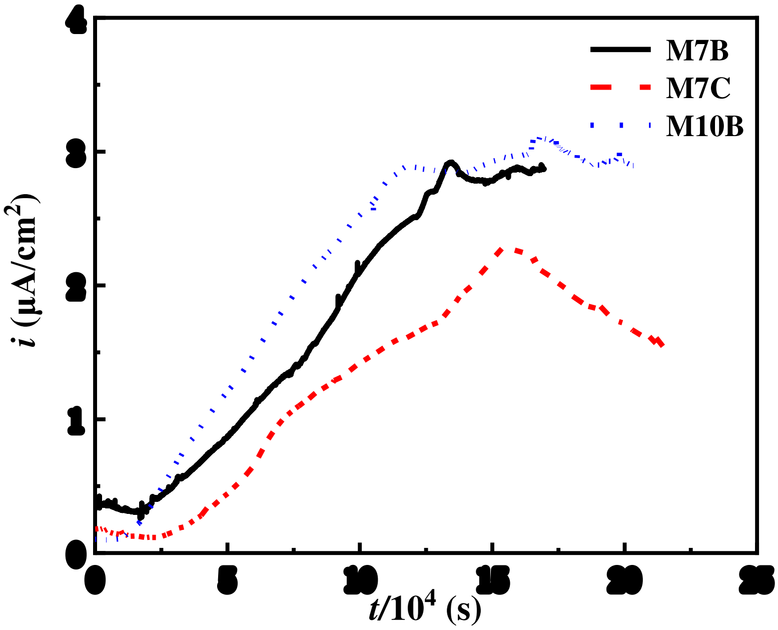

Fig. 7 Hydrogen permeation curves for MMSs

According to microstructure observation and XRD analysis, the main reason for the different hydrogen diffusivity of MMSs is the different volume fraction of austenite. The micrograph of MMSs is characterised by a dual phase consisting of ferrite and austenite. The rate of hydrogen diffusion in ferrite is 4–5 orders of magnitude higher than that in austenite, while hydrogen solubility in austenite is 2–3 orders of magnitude higher than that of ferrite.

Austenite, as a barrier to hydrogen diffusion, leads to a tortuous diffusion path [38], which reduces the diffusion rate of hydrogen in MMSs. The volume fraction of austenite in M10B is higher than that of M7B and M7C.

Table 3 Details of D and $t_{0.63}$ for MMSs

Material	$t_{0.63}$(s)	L(cm)	D(cm^2/s)
M7B	88658	0.128	3.08×10^{-8}
M7C	101538	0.132	2.86×10^{-8}
M10B	73167	0.044	0.441×10^{-8}

3.4 Slow strain rate test with hydrogen charging

Fig. 8 shows the nominal stress – nominal strain curves of MMSs under various hydrogen pre-charged condition. The strain is not measured with a local extensometer but from the cross-head displacement [22]. Therefore, the slope of the linear part of the curve does not correspond to the elastic modules of the steel. The elongation and fracture stress decreased with the increasing time of hydrogen charge from 3 hours to 24 hours. Although the hydrogen charging did not affect the work hardening behaviour much even when the hydrogen embrittlement occurred [30]. For M7B and M10B, due to the presence of a yielding plateau in the strain process, the H-charged samples did not undergo a work-hardening process during the tensile test, with the relatively low fracture stress. The product of strength and elongation decreases rapidly with the increase of hydrogen charging time and hydrogen concentration.

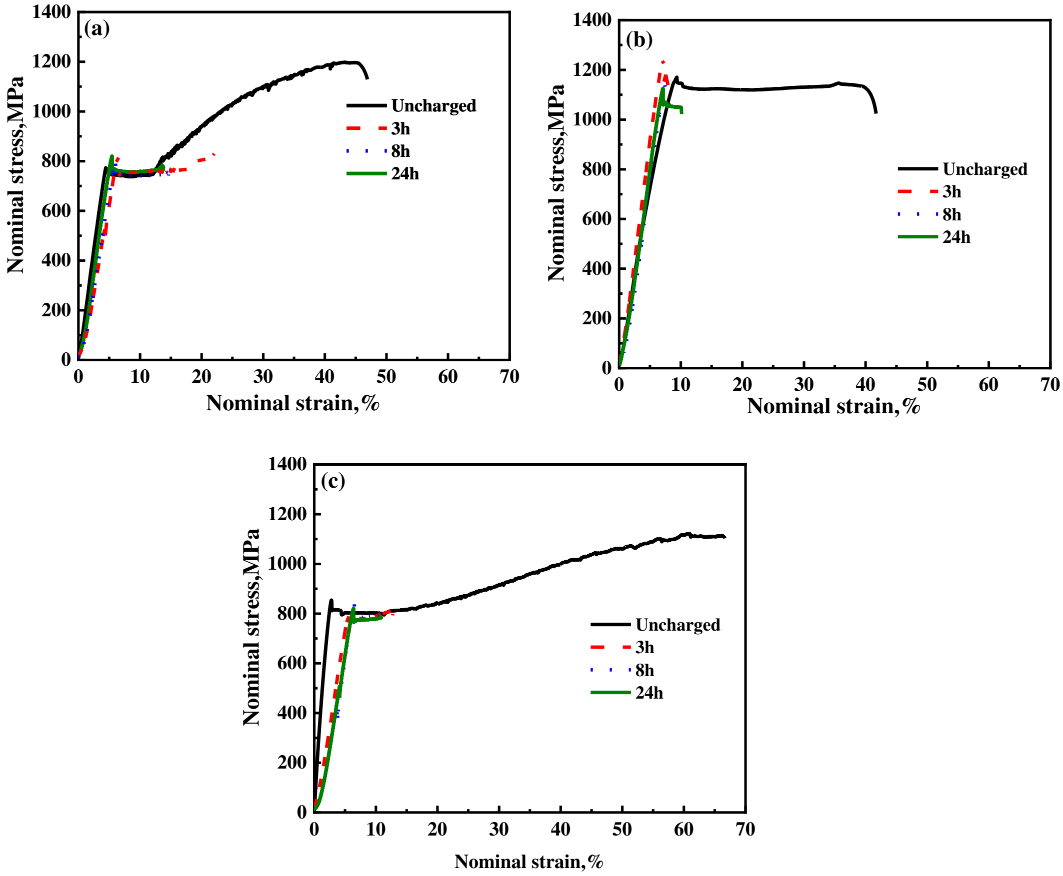

Fig. 8 Stress-strain curves for MMSs under various pre-hydrogen charging SSRT (a) M7B (b) M7C and (c) M10B

The detailed data after SSRT was shown in Table 4, including fracture stress, the loss of ductility and hydrogen concentration. The loss of ductility, one kind of Embrittlement Index representing the sensitivity of HE, can be calculated by the following formula[39].

$$\varepsilon = l_0 - l'$$

$$loss\ of\ ductility = \frac{\varepsilon_0 - \varepsilon_H}{\varepsilon_0} \times 100\%$$

Where l_0: the length of gauge part before SSRT; l': the length of the gauge part after SSRT; ε: the ductility of the specimen; ε_0: the ductility of the specimen in air; ε_H: the ductility of the specimen under hydrogen pre-charged condition;

Fracture stress and elongation as a function of hydrogen content was plotted in Fig 9. Under the same strain rate, fracture stress and ductility decrease gradually with the increase of hydrogen concentration. At the same hydrogen pre-charged condition, as shown in Fig 9, M7C always exhibits highest loss of ductility and the lowest loss of fracture stress among the MMSs. Compared with the hydrogen-uncharged samples, 3-hour hydrogen-charged samples saw a significant degradation of the elongation. So SEM fractographs of MMSs after 3-hour hydrogen pre-charging SSRT were observed as shown in Fig 10. The initiation of cracking and shear lip area of each specimen were observed at high magnifications, exhibiting a brittle fracture mode and secondary cracks observed at the same time. The HE mechanism of MMSs was explained by experimental results and fractograph observations below.

Table 4 Mechanical properties and hydrogen content of the MMSs after SSRT under different pre-charged condition

Steel	condition	Fracture stress/MPa	Ductility/ %	Loss of ductility/ %	The product of TS and ductility/GPa• %	Hydrogen content/wppm
M7B	No charged	1133	31.3	0	35.5	0.15
	Pre-charged 3 hours	830	11.4	60.9	8.8	1.34
	Pre-charged 8 hours	760	10.2	67.4	7.8	3.67
	Pre-charged 24 hours	709	5.1	83.7	3.6	4.42
M7C	No charged	1130	30.4	0	34.3	0.21
	Pre-charged 3 hours	1130	7.9	74.0	9.0	2.56
	Pre-charged 8 hours	1047	6.2	79.6	6.5	4.51
	Pre-charged 24 hours	1022	4.3	85.9	4.4	4.98
M10B	No charged	1403	40.0	0	56.1	0.25
	Pre-charged 3 hours	798	12.7	68.3	10.1	3.1
	Pre-charged 8 hours	793	8.6	78.5	6.8	5.8
	Pre-charged 24 hours	780	5.9	85.3	4.7	24.2

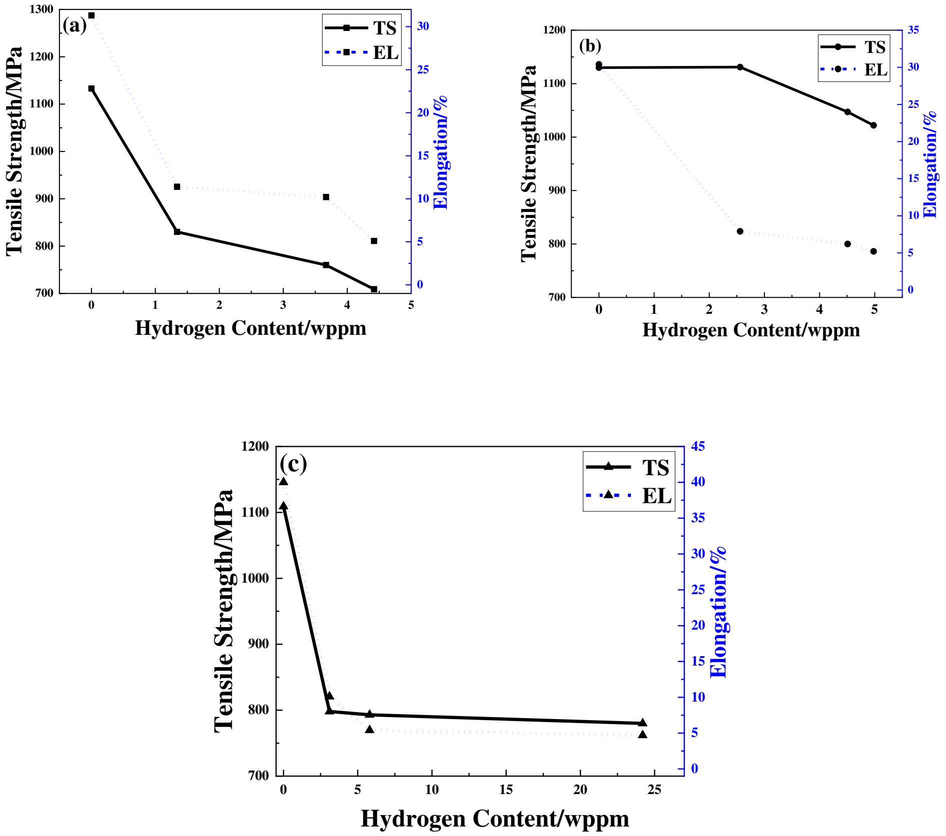

Fig. 9 Tensile strength and elongation as a function of hydrogen content for (a) M7B (b) M7C and (c) M10B

For M7B and M10B, after a lengthy batch-annealing process, the grain is uniformly fine without defects and internal stress, ensuring the adequate diffusion of Mn and C. Due to the entry of diffusible hydrogen, as shown in Fig.9 (a) and (c), the fracture stress and elongation exhibited sharp drop at a certain hydrogen content. This certain content of hydrogen was named ‘critical hydrogen concentration’, making the fracture transition from ductile dominated fracture mode into brittle mode. The critical hydrogen concentration for M7B and M10B, in this study, is 1.34 wppm and 3.10 wppm respectively. The samples after hydrogen-charging shown different fracture surface compared with no hydrogen-charging samples. Compared with Fig.4, fracture surface is smooth without delamination for M7B and M10B in Fig.10 (a) and (i), while obvious delamination for M7C shown in Fig.10 (e). The reason is that the occurrence of delamination is associated with the applied stress exceeding yield strength. But for M7B and M10B, the fracture stress is not big enough to occur plastic deformation degraded by the entry of more hydrogen. According to HEDE mechanism, hydrogen atoms diffuse inwards and enrich at grain boundaries of austenite and decrease the cohesive strength of material at crack tip to form continuous weak bond zone and intergranular fracture occurs in M7B and M10B [16], shown in Fig.10 (c) (d) and (k) (l).

M7C shows different fracture mode from M7B and M10B due to different heat treatment and hydrogen behaviour in material. The various fracture modes, for example, intergranular, quasi-cleavage and dimple might be seen depending on the hydrogen concentration, microstructure and stress intensity of crack tip [16]. The distributed lath-shaped austenite had relatively low stability and it would deformed and transformed into martensite at lower strain condition in M7C. As shown in Fig.3 and Fig.8, the stress of M7C reaches a higher level at `lower strain than that of M7B and M10B whether hydrogen-charging or not. Meanwhile, the yield strength is close to tensile strength. The fracture stress of M7C did not decrease as sharply as that of M7B and M10B after hydrogen-charging process, in Fig.9 (b). Under the circumstances, stress has a dominated effect in fracture modes, consistent with discussion about delamination occurring at stress concentration. It is generally acknowledged that the delamination is the result of the coalescence of micro-cracks induced by stress. According to red box Fig.10 (b) (f) (g), the amount of micro-cracks in M7C is much higher than that in M7B and M10B. That explains that the delamination fracture appeared at half thickness of cross-section in Fig.10 (e) and disappeared in Fig.10 (a) and (i). By fractography examination of M7C after SSRT, shown in Fig.10 (h), it was concluded that the fracture showed the brittle fracture mode at the edge of the specimen and ductile mode characterized with dimples in the centre of the specimen. According to the adsorption-induced dislocation emission (AIDE) and hydrogen assisted micro void coalescence (HDMC) mechanisms, the mixed fracture mode in M7C after SSRT might be cause by the combination of hydrogen content and stress intensity of crack tip. Firstly, hydrogen atoms are adsorbed at the region of stress concentration and results in facilitating dislocation injection from a crack tip and then crack growth and formation of microviods by HELP. The micro-cracks initiation and propagation happened after the joining of microvoids, as shown in Fig.10 (f). The micro-void coalescence dimple produced due to the effect of hydrogen but they possess poor ductility. Final fracture occurs due to shear stress so shear dimple presented, shown in Fig.10 (h). Brittle intergranular fracture can be seen in Fig.10 (g) at the edge of the specimen due to the effect of hydrogen.

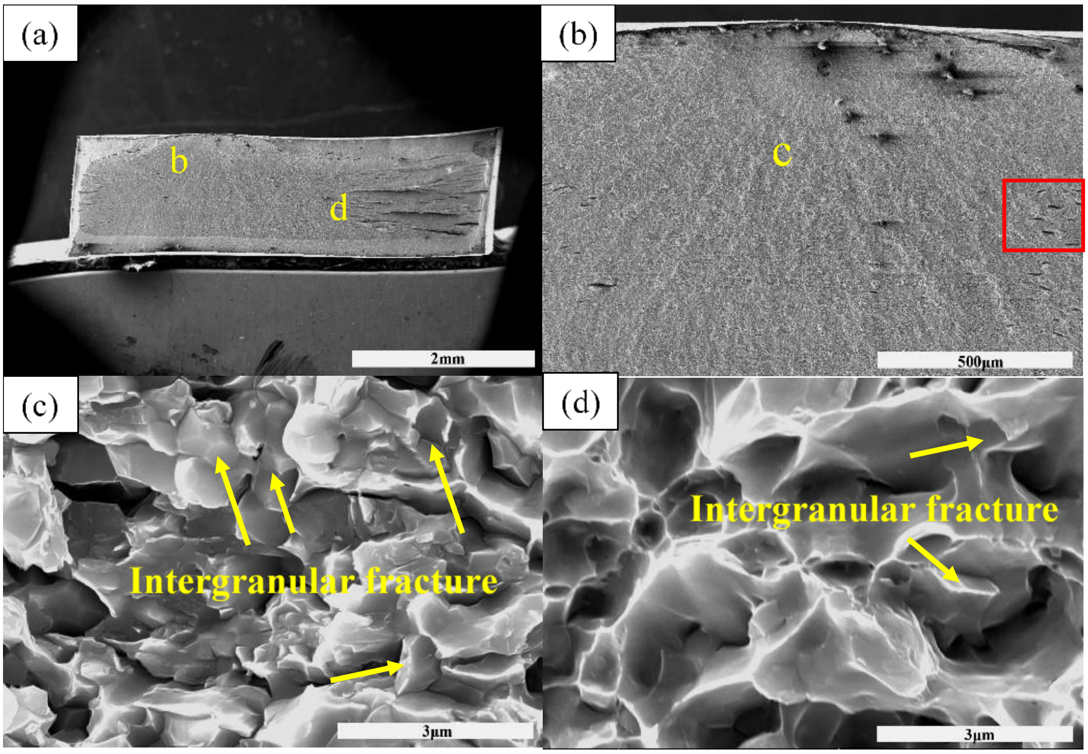

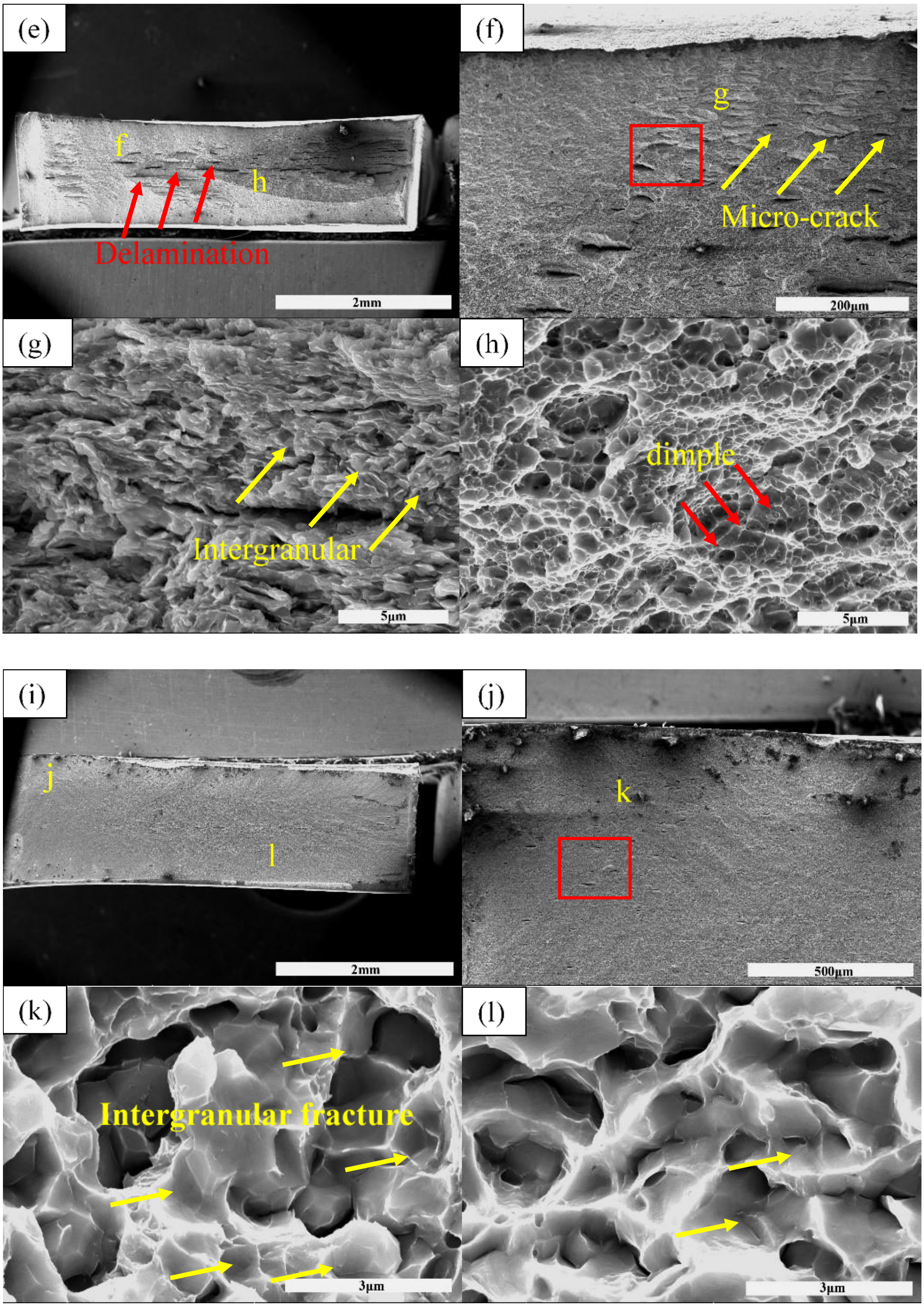

Fig.10 Fracture surfaces of MMSs under 3-hour hydrogen pre-charging SSRT: (a) the whole fracture surface of M7B;(b) (d) magnified image of the part marked in (a); (c) magnified image of the part marked in (b);(e) the whole fracture surface of M7C;(f) (h) magnified image of the part marked in (e) and (g) magnified image of the part marked in (f);(i) the whole fracture surface of M10B;(j) (l) magnified image of the part marked in (i) and (k) magnified image of the part marked in (j);

Retained austenite, as a strong hydrogen trap in MMSs, forces hydrogen to diffuse to the boundary of ferrite and austenite or the interior of austenite. Austenite transforms into martensite during plastic deformation induced by stress. The dissolved hydrogen in austenite would diffuse into the stress concentration position of the matrix and promote the initiation of a microcrack [34]. The fracture propagated quickly with the increase of stress. Observing the fracture, it is found that some dimples filled with grains were generated by intergranular cracking occurring along the boundaries of RA grains or the boundary of the dual phase. The dissolved H in austenite diffuses to the interface during phase transformation, thus reducing the cohesive bonding force between grains. Also, stress concentration at the crack leads to intergranular cracking, which can be explained by the HEDE mechanism. The empty dimples were generated by intragranular cracking occurring at grain boundaries. Hydrogen leads to local deformation by facilitating dislocation emission, causing stress concentration in the crack tip, showing the empty dimple in the fracture morphology.

4. Conclusions

In this paper, the effect of hydrogen concentration on the mechanical properties and fracture behaviour and the interpretation of different HE mechanisms of medium Mn steels (M7B, M7C, M10B) were studied through the hydrogen permeation test and slow strain rate tensile test after hydrogen-charging. The conclusions drawn from this work include the following:

(1) Due to the different heat treatment conditions, the grain size of M7B and M10B is relatively uniform, with a size of 1–3 μm, and the microstructure of M7C retains long strip characteristics. The increase of Mn content increases the volume fraction of RA in the specimen, resulting in a higher fraction of RA in M10B than in M7B and M7C. After a short period of continuous annealing treatment, the stability of austenite in M7C is poor, clearly changing at the beginning of strain. Therefore, the yield strength of M7C is much higher than that of M7B, and there is no work-hardening stage on the stress-strain curve. The RA in M7B and M10B is relatively stable and undergoes a continuous

work-hardening process after the yielding platform.

(2) Austenite content has a decisive influence on hydrogen diffusion rate. As the volume fraction of austenite in M10B is two times that of M7B and M7C, austenite, as a block to hydrogen diffusion, decreases the diffusion rate of hydrogen.

(3) If hydrogen content is more than the critical level of hydrogen which is known as critical hydrogen concentration (H_c), then HE happened in material and seriousness of HE is depend on the amount of hydrogen concentration. The H_c of M7B and M10B was provided based on this study.

(4) The fracture morphology was determined by the combination effect of hydrogen content and applied stress. For M7B and M10B, hydrogen plays a dominated role in determining the brittle fracture after three-hour hydrogen-charging, while the fracture in M7C showed the mixed fracture mode determined by the synergistic action of hydrogen content and stress.

(5) The variety of mechanisms are available and responsible for HE of a material such as HEDE, HELP, AIDE and HDMC. The HE in M7B and M10B can be explained by HEDE mechanism. More than one mechanisms are responsible for degradation and embrittlement of material. To reduce HE phenomena and interpret it clearly, selection of a material is very much important. Even in the same material, the HE mechanism could be different regarding to the region. The fracture surface of M7C showed mixed modes with brittle edge and ductile centre. Still the actual mechanism which causes embrittlement occurs in a material is unclear and research will be going on to identify the main embrittlement causes of a material**.**

Acknowledgement

This work was supported by the National Natural Science Foundation of China [grant NO. U1660104].

References

[1] R.L. Miller, Ultrafine-grained microstructures and mechanical properties of alloy steels, Metallurgical Transactions 3(4) (1972) 905-912.

[2] T. Furukawa, Dependence of strength–ductility characteristics on thermal history in lowcarbon, 5 wt-%Mn steels, Materials Science and Technology 5(5) (1989) 465-470.

[3] L. Luo, W. Li, L. Wang, S. Zhou, X. Jin, Tensile behaviors and deformation mechanism of a medium Mn-TRIP steel at different temperatures, Materials Science and Engineering: A 682 (2017) 698-703.

[4] P.J. Gibbs, E.D. Moor, M.J. Merwin, B. Clausen, J.G. Speer, D.K. Matlock, Austenite Stability Effects on Tensile Behavior of Manganese-Enriched-Austenite Transformation-Induced Plasticity Steel, Metallurgical & Materials Transactions A 42(12) (2011) 3691-3702.

[5] W.S. Dong, J.H. Ryu, S.J. Min, H.S. Yang, K. Lee, H.K.D.H. Bhadeshia, Medium-Alloy Manganese-Rich Transformation-Induced Plasticity Steels, Metallurgical & Materials Transactions A 44(1) (2013) 286-293.

[6] H. Choi, S. Lee, J. Lee, F. Barlat, B.C. De Cooman, Characterization of fracture in medium Mn steel, Materials Science and Engineering: A 687 (2017) 200-210.

[7] Z.C. Li, H. Ding, R.D.K. Misra, Z.H. Cai, H.X. Li, Microstructural evolution and deformation behavior in the Fe-(6, 8.5)Mn-3Al-0.2C TRIP steels, Materials Science & Engineering A 672 (2016) 161-169.

[8] H. Huang, O. Matsumura, T. Furukawa, Retained austenite in low carbon, manganese steel after intercritical heat treatment, Metal Science Journal 10(7) (1994) 621-626.

[9] H. Luo, J. Shi, C. Wang, W. Cao, X. Sun, H. Dong, Experimental and numerical analysis on formation of stable austenite during the intercritical annealing of 5Mn steel, Acta Materialia 59(10) (2011) 4002-4014.

[10] W.Q. Cao, C. Wang, J. Shi, M.Q. Wang, W.J. Hui, H. Dong, Microstructure and mechanical properties of Fe–0.2C–5Mn steel processed by ART-annealing, Materials Science & Engineering A 528(22) (2011) 6661-6666.

[11] J. Han, S.J. Lee, J.G. Jung, Y.K. Lee, The effects of the initial martensite microstructure on the microstructure and tensile properties of intercritically annealed Fe–9Mn–0.05C steel, Acta Materialia 78(2) (2014) 369-377.

[12] S. Thomas, N. Ott, R.F. Schaller, J.A. Yuwono, P. Volovitch, G. Sundararajan, N.V. Medhekar, K. Ogle, J.R. Scully, N. Birbilis, The effect of absorbed hydrogen on the dissolution of steel, Heliyon 2(12) (2016) e00209.

[13] I.M. Robertson, P. Sofronis, A. Nagao, M. Martin, S. Wang, D. Gross, K. Nygren, Hydrogen embrittlement understood, Metallurgical and Materials Transactions A 46(6) (2015) 2323-2341.

[14] R. Oriani, Whitney award lecture—1987: hydrogen—the versatile embrittler, Corrosion 43(7) (1987) 390-397.

[15] J. Venezuela, Q. Liu, M. Zhang, Q. Zhou, A. Atrens, A review of hydrogen embrittlement of martensitic advanced high-strength steels, Corrosion Reviews 34(3) (2016) 153-186.

[16] S.K. Dwivedi, M. Vishwakarma, Hydrogen embrittlement in different materials: A review, International Journal of Hydrogen Energy 43(46) (2018) 21603-21616.

[17] D.H. Herring, Hydroqen embrittlement, Wire Forming Technology International 13(4) (2010) 24-27.

[18] S.K. Dwivedi, M. Vishwakarma, Hydrogen embrittlement in different materials: A review, International Journal of Hydrogen Energy (2018).

[19] Q. Liu, Q. Zhou, J. Venezuela, M. Zhang, A. Atrens, Hydrogen influence on some advanced high-strength steels, Corrosion Science 125 (2017) 114-138.

[20] T. Depover, D. Pérez Escobar, E. Wallaert, Z. Zermout, K. Verbeken, Effect of hydrogen charging on the

mechanical properties of advanced high strength steels, International Journal of Hydrogen Energy 39(9) (2014) 4647-4656.

[21] J. Han, J.-H. Nam, Y.-K. Lee, The mechanism of hydrogen embrittlement in intercritically annealed medium Mn TRIP steel, Acta Materialia 113 (2016) 1-10.

[22] B. Kan, Z.X. Yang, Z. Wang, J.X. Li, Q.J. Zhou, Y.J. Su, L.J. Qiao, A.A. Volinsky, Hydrogen redistribution under stress-induced diffusion and corresponding fracture behaviour of a structural steel, Materials Science and Technology 33(13) (2017) 1539-1547.

[23] J.P. Hirth, Effects of hydrogen on the properties of iron and steel, Metallurgical Transactions A 11(6) (1980) 861-890.

[24] M. Koyama, E. Akiyama, Y.-K. Lee, D. Raabe, K. Tsuzaki, Overview of hydrogen embrittlement in high-Mn steels, International Journal of Hydrogen Energy 42(17) (2017) 12706-12723.

[25] H.K. Birnbaum, P. Sofronis, Hydrogen-enhanced localized plasticity—a mechanism for hydrogen-related fracture, Materials Science & Engineering A 176(1-2) (1994) 191-202.

[26] A. Nagao, C.D. Smith, M. Dadfarnia, P. Sofronis, I.M. Robertson, The role of hydrogen in hydrogen embrittlement fracture of lath martensitic steel, Acta Materialia 60(13) (2012) 5182-5189.

[27] S.P. Lynch, 2 - Hydrogen embrittlement (HE) phenomena and mechanisms, in: V.S. Raja, T. Shoji (Eds.), Stress Corrosion Cracking, Woodhead Publishing2011, pp. 90-130.

[28] M. Nagumo, T. Yagi, H. Saitoh, Deformation-induced defects controlling fracture toughness of steel revealed by tritium desorption behaviors, Acta Materialia 48(4) (2000) 943-951.

[29] M. Nagumo, Hydrogen related failure of steels – a new aspect, Materials Science and Technology 20(8) (2004) 940-950.

[30] M. Koyama, E. Akiyama, K.J.C.S. Tsuzaki, Effect of hydrogen content on the embrittlement in a Fe–Mn–C twinning-induced plasticity steel, 59 (2012) 277-281.

[31] Y. Zhang, L. Wang, K.O. Findley, J.G. Speer, Influence of Temperature and Grain Size on Austenite Stability in Medium Manganese Steels, Metallurgical & Materials Transactions A 48(5) (2017) 1-10.

[32] ASTM E8 / E8M-16a, Standard Test Methods for Tension Testing of Metallic Materials, ASTM International, West Conshohocken, PA, 2016, www.astm.org.

[33] J. Andersons, M. König, Dependence of fracture toughness of composite laminates on interface ply orientations and delamination growth direction, Composites Science and Technology 64(13) (2004) 2139-2152.

[34] S. Liu, X. Li, H. Guo, S. Yang, X. Wang, C. Shang, R.D.K. Misra, Selective role of bainitic lath boundary in influencing slip systems and consequent deformation mechanisms and delamination in high-strength low-alloy steel, Philosophical Magazine 98 (2018) 1-25.

[35] J. Tao, S. Hu, F. Yan, Y. Zhang, M. Langley, A study of the mechanism of delamination fracture in bainitic magnetic yoke steel, Materials & Design 108 (2016) 429-439.

[36] J.H. Ryu, Y.S. Chun, C.S. Lee, H.K.D.H. Bhadeshia, D.W. Suh, Effect of deformation on hydrogen trapping and effusion in TRIP-assisted steel, Acta Materialia 60(10) (2012) 4085-4092.

[37] T.K. Shan, S.H. Li, W.G. Zhang, Z.G. Xu, Prediction of martensitic transformation and deformation behavior in the TRIP steel sheet forming, Materials & Design 29(9) (2008) 1810-1816.

[38] E. Owczarek, T. Zakroczymski, Hydrogen transport in a duplex stainless steel, Acta Materialia 48(12) (2000) 3059-3070.

[39] F. Cusenza, S. Ringeval, S. Thiébaut, F. Buy, T. Paris, I. Moro, L. Briottet, V. Vignal, Study of the Hydrogen Embrittlement Sensitivity of an X4CrNiMo 16.5.1 Stainless Steel and the Associated Electron Beam Weld, ASME 2015 Pressure Vessels and Piping Conference, 2015.